

# Topological transition in cyanobacteria: from motion to structure

Jan Cammann,<sup>1</sup> Mixon K. Faluwiki,<sup>2,3</sup> Nayara Dambacher,<sup>2,4</sup> Lucas Goehring,<sup>2,\*</sup> and Marco G. Mazza<sup>1,†</sup>

<sup>1</sup>*Interdisciplinary Centre for Mathematical Modelling and Department of Mathematical Sciences, Loughborough University, Loughborough, Leicestershire LE11 3TU, United Kingdom*

<sup>2</sup>*School of Science and Technology, Nottingham Trent University, Nottingham NG11 8NS, UK*

<sup>3</sup>*Malawi Institute of Technology, Malawi University of Science and Technology, S150 Road, Thyolo 310105, Malawi*

<sup>4</sup>*School of Biosciences, University of Nottingham, Sutton Bonington Campus, LE12 5RD, UK*

Many active systems are capable of forming intriguing patterns at scales significantly larger than the size of their individual constituents. We recently introduced a model for gliding filamentous cyanobacteria, which form a reticulate pattern as an early-stage biofilm. Our observations reveal that the filaments' bodies follow the track of the head, and are subject to curvature fluctuations, defining a new class of active matter: active spaghetti. By identifying the dominant aspects of the filament's dynamics, our model achieves great computational efficiency, without coarse-graining past the scale of an individual filament. Here, we explore large-scale collective effects and rich dynamics of cyanobacteria colonies, while still retaining information about the individual constituents' dynamics and their interactions. We characterize the system's topological transition from an isotropic distribution to a state of large-scale reticulate patterns by quantifying both dynamical and structural observables. Although it is not a periodic structure, in the steady state the reticulate pattern possesses a well-defined length scale determined by the filaments' Péclet number, which controls the relative importance of activity and curvature fluctuations.

## INTRODUCTION

Living matter is fundamentally characterized by its ability to self-organize [1–4]. This is visible at length scales spanning a staggering range of about nine orders of magnitude, from the few microns of the complex structures present inside a eukaryotic cell, such as its nucleus, the endoplasmic reticulum, or the length of a microtubule, [5–7] to the complex spatial organization in bacterial biofilms extending over millimeters [8–10], to the scale of flocks of birds [11, 12] or schools of fish [13], up to kilometer-long herds of wildebeest [14, 15]. Starting from the seminal work of Vicsek *et al.* [16], the self-organization of large collectives of simple objects has garnered considerable interest within the field of active matter [16–25]. Active systems are defined by the injection of energy into individual elements, which is converted into directed motion [26]. This energy injection explicitly breaks time-reversal symmetry [27] and allows active matter systems to exhibit emergent properties not observable in equilibrium systems [20, 21].

A simplifying assumption involved in the modeling of many active-matter systems is to treat their basic components as point-like particles [16, 17, 19] or stiff rods [28–30], each with its own orientation, and a few rules for their motion and pairwise interactions. Archetypes of these systems are the Vicsek model [16, 31, 32], the active Brownian particle model [33–35], where self-propelled particles interact with neighbors via spherically-symmetric steric repulsion, and the active nematic model [36, 37], where filaments are described with a single orientation, in analogy to liquid crystal molecules.

In contrast, long, flexible filaments such as microtubules or active polymers are typically described by an

orientation  $\theta$  that varies along their arc length  $s$ . Their dynamics are then commonly modeled using techniques adopted from polymer physics [38–54], where filaments are represented by discrete monomers connected together through bonding potentials, allowing each link within the chain to have its own laws of motion.

Cyanobacteria are one of the most important [55–57] and ancient [58, 59] groups of species to have evolved on Earth, with evidence of their presence in the fossil record dating back to at least two billion years ago [60, 61]. Their ancestors first evolved oxygenic photosynthesis [57], which changed the chemical composition of the atmosphere, thus paving the way for the evolution of animals. In green plants and eukaryotic algae photosynthesis is carried out in the plastids, organelles now recognized to be endosymbiotic cyanobacteria, one of the two major examples of endosymbiosis in the history of life [62] (the other is the case of mitochondria). In terms of sheer number of cells, cyanobacteria are also the most common type of life that has ever lived [63]. They are found in extreme environments like hot springs, deserts and the polar regions [64], but also in everyday streams and fountains. A particularly diverse prokaryotic phylum, species of cyanobacteria range from unicellular to multicellular filamentous and branching forms [61, 65].

Filamentous cyanobacteria grow as long hair-like chains of cells called trichomes, see Fig. 1(a), and are a particularly important type of microorganism; for example, they dominate the ecology of shallow lakes [66], and due to their size and structure they can be used in wastewater management more efficiently than unicellular microbes [67]. Numerous species of filamentous cyanobacteria exhibit gliding motility, which is instrumental in the formation of biomats [68, 69].

These gliding cyanobacteria are becoming recognized

as the archetype of a distinct class of active filaments [70–74]. Unlike active polymers, their motion cannot be represented as resulting from active forces tangential to monomer-like elements [49, 75]. Gliding cyanobacteria exert negligible forces on each other, as opposed to the stresses that they apply on their substrate, which represents a very different physical case than active nematics based on microtubule-kinesin or actin-myosin [76]. The physical properties that set gliding cyanobacteria apart from other active filament systems, and which help define their own class of active matter, active spaghetti, include: (i) a large aspect ratio, (ii) gliding motility induced by polar forces, (iii) path-tracking dynamics, where the body of the filament follows the track laid down by its head (also known as metameric locomotion [52]), and (iv) non-reciprocal aligning interactions.

Cyanobacteria can form biomats [77], and their elongated species can form reticulate biomats [69, 78]. Their reticulate features are irregular network-like patterns emerging from the self-organization of trichomes first into dense bundles and then into a network topology. These patterns contribute to rapid collective responses [79, 80], mechanical properties [69] and act as a template for more complex 3D structures [69, 81]. We recently studied the reticulate network that emerges as a self-organized pattern of gliding filamentous cyanobacteria [70]. The characteristic scale of this network is determined by a balance of activity and fluctuations [70].

Here, we explore the dynamics, structure, and phase behavior of a system of active filaments, modeled after the behavior of cyanobacteria. We investigate the large-scale collective effects of cyanobacteria colonies, while still retaining information about the individual constituents’ dynamics and their interactions. Combining numerical simulations with theoretical arguments, we uncover a rich dynamics for this model of gliding filaments as their Péclet number  $Pe$ , density, and length are varied. As it develops towards a statistically steady state, this model shows transient behaviors that closely resemble corresponding experiments with filamentous cyanobacteria. We also find that the filaments’ effective translational diffusivity grows with the Péclet number,  $Pe$ . The nonequilibrium phase diagram of the system exhibits a transition from isotropic to reticulate patterns as  $Pe$  and the area coverage, or density, increase. Finally, inspired by polymer physics, we compute the parallel and perpendicular pair correlation function for the filaments. The features of these correlation functions carries information about the structure of the reticulate network and faithfully predicts its characteristic length scale.

Taken together, our results identify the curvature fluctuations and aligning interactions as the mechanism underpinning the nonequilibrium transition to the reticulate pattern in filamentous cyanobacteria.

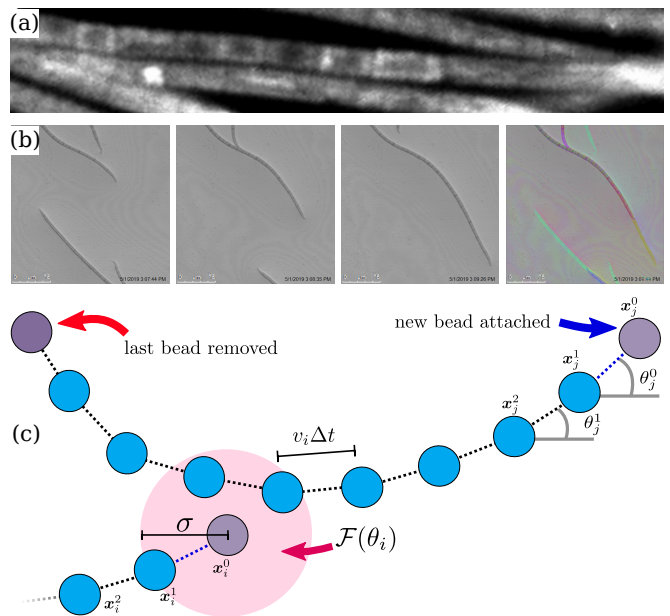


FIG. 1. Dynamics of gliding motility. (a) Close-up micrograph of *Oscillatoria lutea* filaments, composed of a chains of individual cells. (b) A time lapse of three micrographs demonstrates filament motion, by which each filament’s body glides along the track laid down by its head. The rightmost image highlights this path-tracking dynamics by overlaying the three images using shadings of different colors. (c) Schematic depiction of the model filaments, as discretized into chains of connected beads. Beads are placed at a fixed distance  $v_i \Delta t$  apart. Upon advancing time by an increment  $\Delta t$ , the last bead of a filament is removed and placed as its new head. Non-reciprocal interactions occur when a filament’s head (filament  $i$ ) is within a distance  $\sigma$  from any bead of another filament,  $j$ . The head experiences a nematic aligning interaction  $\mathcal{F}(\theta_i)$  while filament  $j$  remains unaffected by this interaction.

## RESULTS

### Model for gliding cyanobacteria

Empirical observations guide the development of our model of the gliding motion of cyanobacteria, which then predicts the emergent behavior of cyanobacteria colonies. When gliding on surfaces, the head of a trichome lays out a path that the rest of the filament follows very closely; this is an analogue of the metameric motion observed in segmented animals, such as annelids and myriapods [52]. Figure 1(b) shows a time-series of micrographs of *Oscillatoria lutea*, which are then overlaid to demonstrate how the body of each filament follows the track of its head. To capture this behavior, we discretize the trichomes as chains of connected beads. In contrast to active polymer models, however, these beads do not have active forces applied tangent to the length of the filament, nor is there an independent random force (e.g. thermal noise) on each bead, nor any reaction force. Rather, the only forces rel-

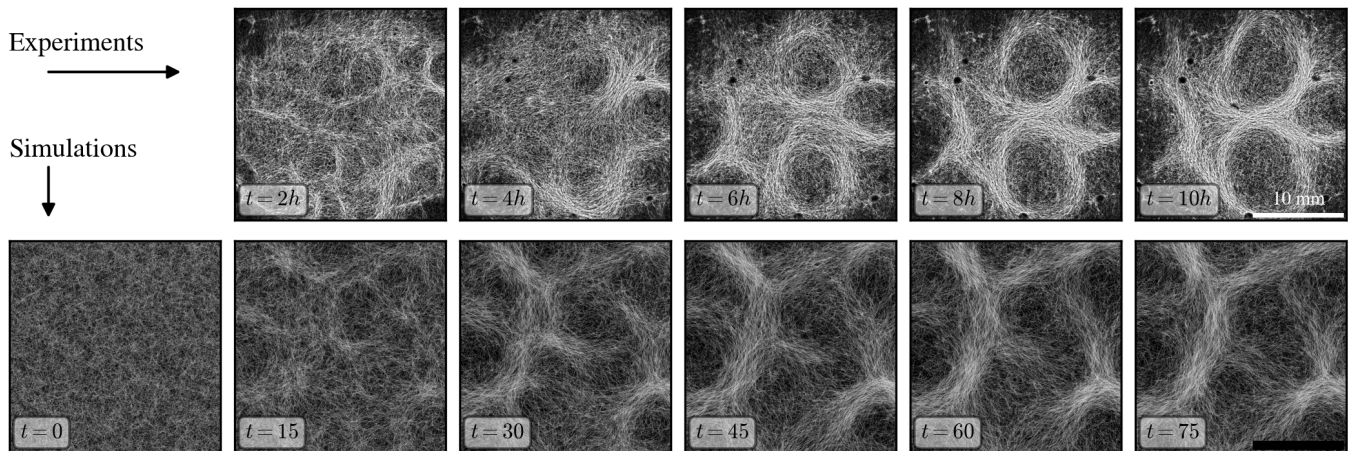


FIG. 2. Time evolution of systems of filaments forming into reticulate structures. The top row shows observations of experiments performed with *Oscillatoria lutea*, where  $v_0 = 3 \mu\text{m/s}$  and  $\tau = 8 \text{ min}$  [70]. The lower panels show simulations of a system initialized with randomly oriented filaments at  $t = 0$ , using a filament length of  $L = 1$ , a Péclet number of  $\text{Pe} = 3.5$  and an area coverage of  $\Phi = 1$ . The field of view shown and time between snapshots match the experimental measurements of *O. lutea* (i.e.  $t = 15$  corresponds to 2 hours). In both cases the initial pattern forms with smaller features that coarsen slightly to achieve a stable length scale over a period of a few hours ( $t \approx 50$ ).

evant to the motion of a filament are those applied to its head. A filament moving at a constant gliding speed  $v_i$  is then modeled as a string of beads with a fixed spacing  $v_i \Delta t$ , where  $\Delta t$  is the time step of the numerical integration. To advance the filament by one time step, we remove the last bead in the chain (the tail), and add a new bead to the head. A similar approach has been taken to study the dynamics of isolated filaments [52], and of filaments on a lattice [76]. In this way, for each bead  $\alpha$  on any filament  $i$  the resulting path-tracking motion for the beads' positions  $\mathbf{x}_i^\alpha$  can be expressed as

$$\mathbf{x}_i^\alpha(t) = \mathbf{x}_i^{\alpha-1}(t - \Delta t), \quad (1)$$

for all beads except the filament's head,  $\alpha = 0$ , as sketched in Fig. 1(c).

The head bead ( $\alpha = 0$ ) is where interactions take place, and so is treated separately. Dropping the index  $\alpha$ , a filament's head moves forward at a fixed speed,

$$\frac{d\mathbf{x}_i}{dt} = v_i \hat{\mathbf{t}}_i. \quad (2)$$

Here,  $\hat{\mathbf{t}}_i \equiv (\cos \theta_i, \sin \theta_i)^T$  is the unit vector tangent to the filament at the head's position, and defines the head's orientation  $\theta_i$ . The gliding speed  $v_i$  of each filament is constant in time, and drawn from a normal distribution with average  $v_0$  and standard deviation  $\delta v$ ; this is in agreement with experimental observations [70], and avoids spurious synchronization effects.

The gliding motion of cyanobacteria is characterized by continuous functions for the orientation and curvature of the filaments. Because the curvature is mathematically well defined and empirically measurable, a simple Brownian process for the angle  $\theta$  is not appropriate; rather,

we use a modified Ornstein–Uhlenbeck process to capture the curvature diffusion of the filament paths [70]. In this case, the angular speed  $\omega_i$  and orientation  $\theta_i$  of the head of filament  $i$  evolve as

$$\frac{d\omega_i}{dt} = -\frac{1}{\tau} \frac{d\theta_i}{dt} + \sqrt{2D_\omega} \xi(t) \quad (3)$$

$$\frac{d\theta_i}{dt} = \omega_i - J\mathcal{F}(\theta_i), \quad (4)$$

where  $\tau$  is the curvature autocorrelation time,  $D_\omega$  is a diffusion coefficient quantifying the strength of the fluctuations in curvature, and  $\xi_i(t)$  is a Gaussian white noise with zero mean and unit variance,  $\langle \xi(t) \rangle = 0$ ,  $\langle \xi(t) \xi(t') \rangle = \delta(t - t')$ .

The last term in Eq. (4) describes the interactions, of strength  $J$ , between nearby filaments, where  $\mathcal{F}(\theta_i) = N_{ij}^{-1} \frac{\partial}{\partial \theta_i} \sum_{i \sim j} \cos(\theta_i - \theta_j^\alpha)$  is a Lebwohl–Lasher interaction inducing nematic alignment between the filaments,  $N_{ij}$  is the number of filaments within an interaction distance  $\sigma$  of the  $i$ -th filament's head,  $\sum_{i \sim j}$  denotes the sum over these filaments, and the orientation angle  $\theta_j^\alpha$  of the bead closest to the  $i$ -th head  $\mathbf{x}_i$ . The interaction has a short, finite range  $\sigma$ , which is consistent with the filaments' effective diameter; when the distance between the head of filament  $i$  and any bead of filament  $j$  is less than  $\sigma$ , the orientation of the head of filament  $i$  undergoes a deflection due to the Lebwohl–Lasher interaction, however, the bead of filament  $j$  remains unperturbed. This makes the interactions fundamentally non-reciprocal, and it is predicated on the experimental observation that when two trichomes meet, only the incident filament's head participates in the alignment process, while the other filament is not deflected [70]. Non-reciprocal interactions explicitly break detailed balance

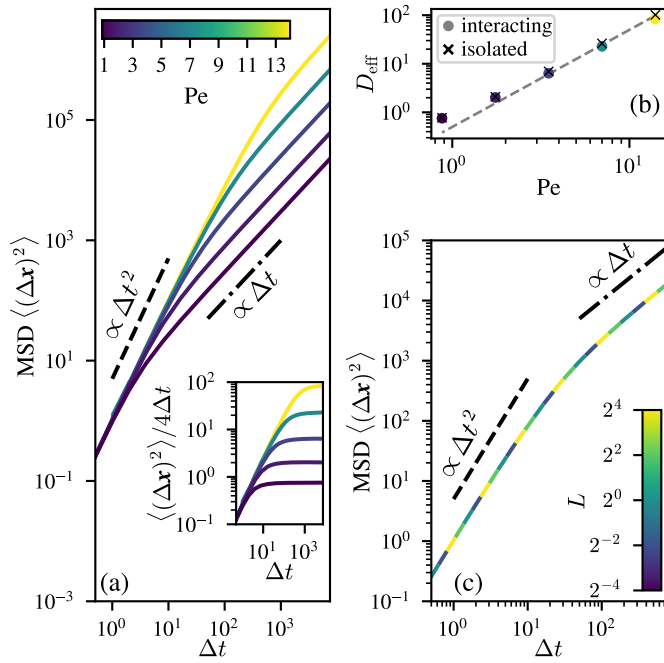


FIG. 3. Characterizing filament motion in simulations. (a) The mean square displacement (MSD) of the filaments' heads exhibits clear ballistic and diffusive regimes, as shown here for different Pe at fixed  $\Phi = 1$  and  $L = 1$ . The inset shows how the MSD converges to a long-time diffusive behavior,  $\langle (\Delta x)^2 \rangle \rightarrow 4D_{\text{eff}}\Delta t$ . This implies that filaments meander throughout the network, rather than being trapped within specific looped paths. (b) The effective translational diffusion coefficient increases with Péclet number for the fully interacting system, and is consistent with the case of noninteracting filaments ( $g = 0$  in Eq. (7)); the dashed line represents the relation  $D_{\text{eff}} = \frac{1}{2}v_0^2\text{Pe}^2$ . (c) Filament length has no discernible effect on the MSD, as shown here for the case of  $\text{Pe} = 3.5$ .

[82, 83] and are common in living active matter [84]. A schematic depiction of the non-reciprocal nematic interactions used in our model is shown in Fig. 1(c).

Without any filament-filament interactions, Eqs. (3)-(4) produce a normal distribution of angular velocities with zero mean and variance  $\langle \omega^2 \rangle = D_\omega\tau$ . For noninteracting filaments moving at an average speed  $v_0$  this translates into a distribution of filament curvatures with zero mean and standard deviation  $\delta\kappa = \sqrt{\langle \omega^2 \rangle}/v_0 = \sqrt{D_\omega\tau}/v_0$ .

To explore the general state diagram of our system, we nondimensionalize the equations of motion by setting  $t = t_0\tilde{t}$ ,  $\mathbf{x} = x_0\tilde{\mathbf{x}}$ , and by choosing  $t_0 = \tau$ , the autocorrelation time, as the characteristic unit of time, and  $x_0 = v_0\tau$  as the characteristic length. The nondimensional equations

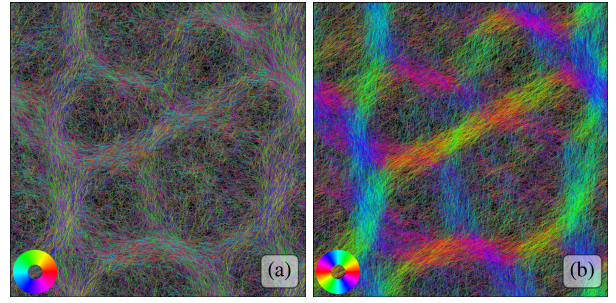


FIG. 4. The reticulate bundles are nematic in nature. The two panels show the same reticulate pattern, with filaments colored according to their local tangent (orientation) using (a) polar and (b) nematic mappings. For the polar case, no preferential direction is discernible within the filament bundles. In the nematic mapping, where orientations  $\theta$  and  $\theta + \pi$  are assigned the same color, the bundles appear in bright colors, highlighting their nematic structure.

of motion read

$$\frac{d\tilde{\mathbf{x}}}{d\tilde{t}} = \tilde{v}_i\hat{\mathbf{t}}_i \quad (5)$$

$$\frac{d\tilde{\omega}_i}{d\tilde{t}} = -\frac{d\theta_i}{d\tilde{t}} + \frac{\sqrt{2}}{\text{Pe}}\tilde{\xi}(\tilde{t}) \quad (6)$$

$$\frac{d\theta_i}{d\tilde{t}} = \tilde{\omega}_i - g\mathcal{F}(\theta_i) \quad (7)$$

where  $\tilde{v}_i = v_i/v_0$ , the dimensionless interaction rate  $g = J\tau$ , and the Péclet number is defined as  $\text{Pe} = (v_0\tau\delta\kappa)^{-1}$ . In our dimensionless units Pe coincides with  $(\delta\kappa)^{-1}$ . In the following, we will drop the tilde signs for ease of notation.

We perform large scale simulation of up to  $N_t = 1\,440\,000$  trichomes in a two-dimensional (2D) domain of size  $L_x = 30$  and area  $A = L_x^2$ , for varying area coverage  $\Phi = \rho L(2\sigma)$  where  $\rho = N_t/A$ . We employ periodic boundary conditions. We fix the width of the self-propulsion speed distribution as  $\delta v = 0.25$ , the interaction range  $\sigma = 0.005$  and an interaction strength  $g = 2$ . Given our choices of parameters, each filament is discretized with 1000 beads, on average. For simplicity, filaments are initially straight, but they rapidly (i.e. over timescales  $t \simeq 1$ ) develop curvature due to noise and alignment effects. Note that area coverage  $\Phi > 1$  is possible, as there are no excluded volume effects; we explore a range of  $0.25 \leq \Phi \leq 1.25$  in our simulations.

Equations (6) and (7) are discretized in time using the Euler-Maruyama method with a timestep of  $\Delta t = 10^{-3}$  while equation (5) is discretized as discussed above and shown in Fig. 1.

## Dynamics and transient

We first investigate the dynamical aspects of the collective self-organization of cyanobacteria filaments. At

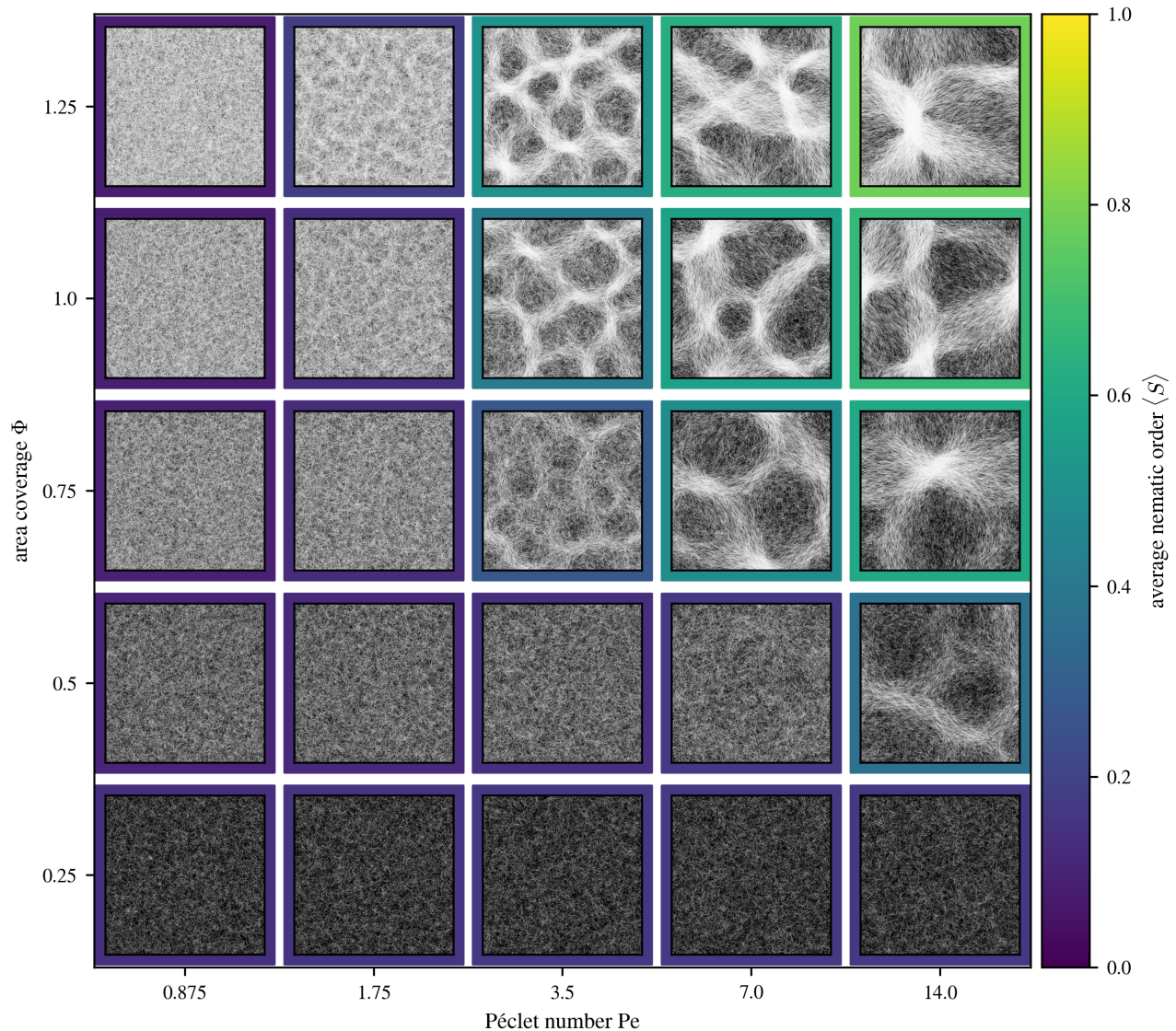


FIG. 5. Collective behavior of the system at different area coverage  $\Phi$  and Péclet numbers  $Pe$ . The individual panels show simulation snapshots at  $t = 150$  in a  $30 \times 30$  domain with periodic boundary conditions. Filament length is kept constant at  $L = 1$ . The panels' frames indicate the system's average nematic order  $\langle S \rangle$ , calculated as an average of  $1 \times 1$  sized blocks. With increasing Péclet number  $Pe$  the system transitions from a disordered state into one showing reticulate patterns of nematic bundles.

sufficiently large number density  $\rho$  and Péclet number  $Pe$  trichomes self-organize into reticulate patterns [59, 70] as shown in Fig. 2. We study here the process by which this reticulate pattern emerges from an isotropic initial condition, and compare model predictions of the transient dynamics with experimental data. In simulations,

we prepare a system of filaments at area coverage  $\Phi = 1$  with a homogeneous distribution of filaments positions and isotropic distribution of their orientations, see Fig. 2.

In experiments, *Oscillatoria lutea* (SAG 1459-3) was cultivated in a medium of BG11 broth diluted 1:100 with deionised water, at  $20 \pm 1^\circ\text{C}$  with a  $10 \pm 2 \mu\text{mol m}^{-2} \text{s}^{-1}$

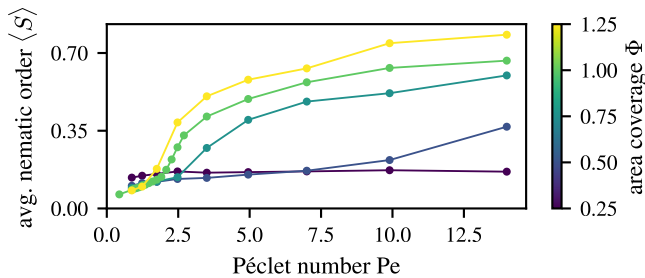


FIG. 6. Average nematic order parameter  $\langle S \rangle$  as a function of Péclet number, calculated as an average of  $1 \times 1$  sized blocks at different area coverages  $\Phi$ . The filament length is kept constant at  $L = 1$ . With increasing  $\Phi$  the transition from disorder to order happens at lower Péclet numbers  $Pe$ .

photon flux on a 16 h day + 8 h night cycle, following Ref. [70]. For imaging, cultures were dispersed by gentle agitation and added dropwise into a 6-well plate (34 mm well diameter), three-quarters filled with medium. Tile-scans of the well were collected every 30 minutes using a confocal laser scanning microscope (Leica TCS SP5) in fluorescence mode (514 nm excitation, 620–780 nm observation). Images of the colony dynamics were cropped and contrast-enhanced to show the central  $17 \times 17$  mm<sup>2</sup> of the well plate, and are given in Fig. 2.

In both experiments and simulations, the aligning interactions lead to the formation of short, dense bundles of filaments. Over time, these bundles connect and self-organize into a network topology. During an initial transient period, the typical separation length between bundles, which provides a characteristic length scale for the patterns, slowly coarsens. After a few hours in the experiments, or simulation times of  $t \sim 50$ , the pattern then converges into a steady-state configuration of reticulate bundles of high local density, with less dense regions in between. The comparison of the transient dynamics between experiments and simulations reveals that our model quantitatively reproduces the emergence of the reticulate pattern in time; in fact, for  $\tau = 8$  min, as measured in Ref. [70] a simulated time  $t = 75$  corresponds to 10 hours, which allows for a direct, one-to-one comparison to the experimental time scale, as in Fig. 2.

To characterize the dynamics of the filaments, we next consider their translational mean square displacement (MSD), defined as

$$\langle (\Delta \mathbf{x})^2 \rangle = \left\langle \frac{1}{N_t} \sum_{i=1}^{N_t} |\mathbf{x}_i(t_0 + \Delta t) - \mathbf{x}_i(t_0)|^2 \right\rangle, \quad (8)$$

where the angular brackets indicate an average over initial times  $t_0$ . The MSD for a polymeric filament can in principle be computed for any part of the filaments, but here, for simplicity, we only use only the positions of the filament heads,  $\mathbf{x}_i(t)$ . Figure 3(a) shows the dependence of the MSD on the observation interval  $\Delta t$ . Over

short periods there is a ballistic regime, where the MSD grows as  $\langle (\Delta \mathbf{x})^2 \rangle \propto (\Delta t)^2$ . On longer timescales, the MSD exhibits a crossover to a diffusive regime, where  $\langle (\Delta \mathbf{x})^2 \rangle = 4D_{\text{eff}} \Delta t$ , for an effective translational diffusion constant  $D_{\text{eff}}$ . The inset to Fig. 3(a) shows that our simulations have comfortably reached this diffusive regime, since  $\langle (\Delta \mathbf{x})^2 \rangle / 4\Delta t \rightarrow \text{const.}$  Figure 3(a) also shows the dependence of the MSD on the Péclet number  $Pe$ . As  $Pe$  increases, the crossover time between the ballistic and diffusive regimes grows as  $t_{\times} = 4D_{\text{eff}}/v_0^2$ . Furthermore, the effective diffusivity  $D_{\text{eff}}$  grows with  $Pe$ , as detailed in Fig. 3(b). To a good approximation we find that  $D_{\text{eff}}$  increases quadratically with  $Pe$ , and more specifically as  $D_{\text{eff}} = \frac{1}{2}v_0^2Pe^2$ , shown as a dashed line in Fig. 3(b).

It is interesting to compare these results with the behavior of 2D active Brownian particles, whose effective diffusivity  $D_{\text{eff}}^{\text{ABP}} = D_T + \frac{v_0^2}{2D_R}$ , where  $D_T$  and  $D_R$  are the translational and rotational diffusion coefficients, respectively [85]. From our definitions of the Péclet number and  $\delta\kappa$  it follows that  $Pe = (D_{\omega}\tau^3)^{-1/2}$ . Setting  $D_T \simeq 0$  and identifying  $D_R \simeq D_{\omega}\tau^3$ , we can identify that  $D_{\text{eff}} = \frac{1}{2}v_0^2Pe^2$ . This prediction is in good agreement with the simulation results. Figure 3(b) also shows that switching off the interactions among filaments, i.e. setting  $g = 0$  (which removes the possibility to form bundles), does not affect their translational diffusivity. In other words, the presence of the reticulate pattern does not impede the motility of the filaments; that implies that the filaments do not remain confined within any particular bundle, loop, or other local feature. We note that these results deviate from the prediction of  $D_{\text{eff}} \propto Pe^2$  at small values of  $Pe$ . This is due to the large values of  $\delta\kappa$ , that is, the filaments experience a broad range of rotational diffusivities. It is also worth mentioning that our model does not predict any dependence of the MSD on the length  $L$  of the filaments, as shown in Fig. 3(c).

While the filaments' gliding motility is of polar nature, the nematic nature of their interactions results in the nematic symmetry within the bundles, with filaments moving along them in either direction in equal parts, see Fig. 4. The approximate equal distribution of orientations within bundles was also measured experimentally in Ref. [70]. While the resulting patterns may look reminiscent of vortex lattices observed in other active systems, the filaments are not constrained to vortices and explore the paths formed by the network of bundles.

## Structure

We now turn to the investigation of the structural properties of the reticulate pattern. Given the nematic nature of the bundles (Fig. 4), and the fact that they can emerge from an isotropic distribution of filament orientations (Fig. 2), we quantify the topological transition

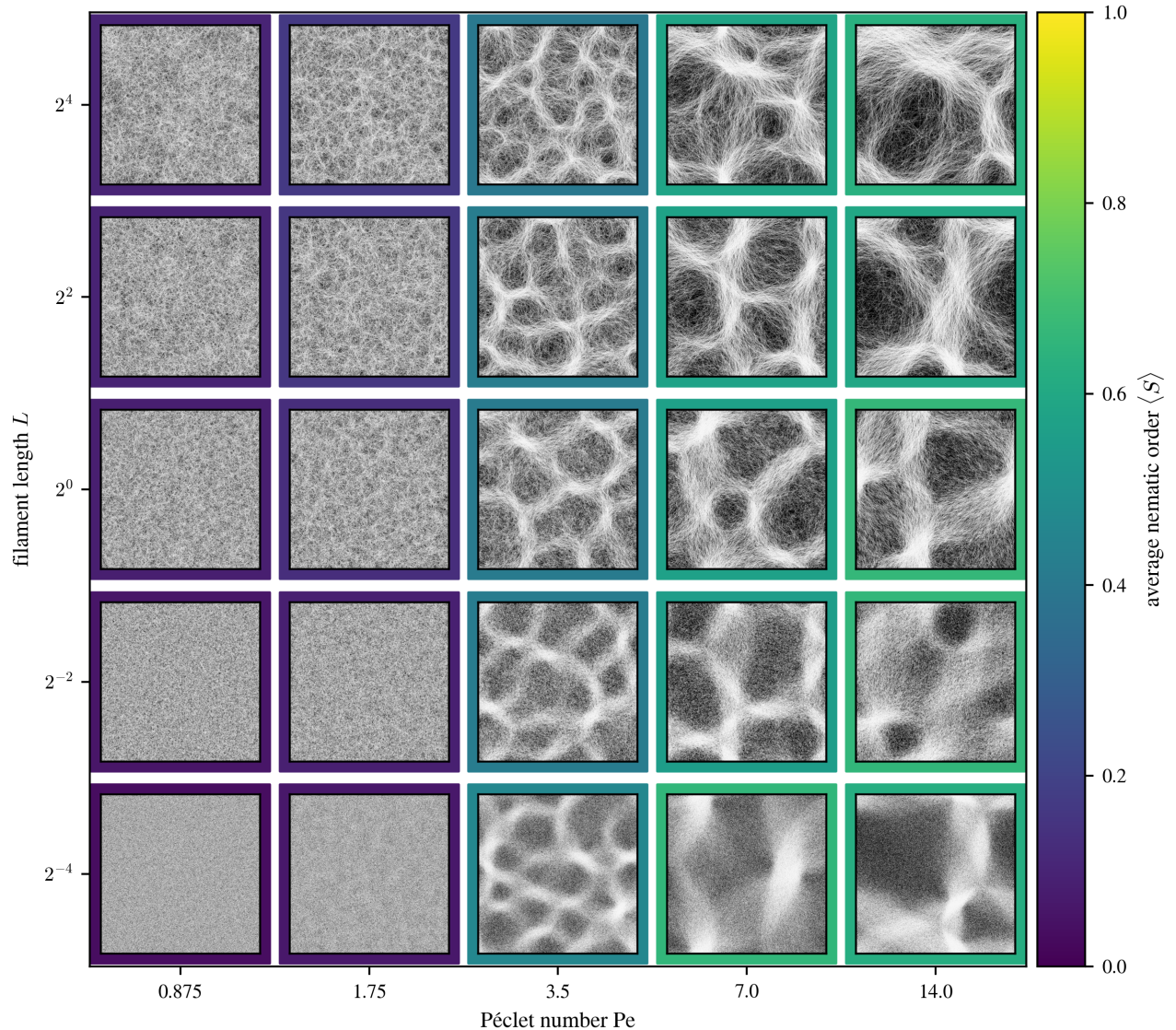


FIG. 7. Collective behavior of the system for different filament lengths  $L$  and Péclet numbers  $Pe$ . The individual panels show simulation snapshots at  $t = 150$  in a  $30 \times 30$  domain with periodic boundary conditions. The density of simulations is set to ensure an equal area coverage, such that  $\Phi = 1$ . The panels' frames indicate the system's average nematic order  $\langle S \rangle$ , calculated as an average of  $1 \times 1$  sized blocks. With increasing Péclet number  $Pe$  the system transitions from a disordered state into one showing reticulate patterns of nematic bundles. The length scale of the emerging patterns is not affected by filament length.

to the reticulate network topology using the 2D nematic order parameter  $\langle S \rangle = \langle \cos(2\hat{\theta}) \rangle$ . To calculate  $\langle S \rangle$ , we sample the local orientation  $\hat{\theta}$  of every filament at  $160L$  regularly spaced points along the filaments' length  $L$ , and calculate  $\langle S \rangle$  as a block average within blocks of size  $1 \times 1$ . Here,  $\hat{\theta}$  is now the filaments' local orientation, relative to

the average orientation, or director, in each block. At this scale, the filament density is relatively homogeneous, but the blocks are large enough to provide good statistics.

Figure 5 shows snapshots of the steady state of simulations at different Péclet number  $Pe$  and area coverage  $\Phi$ . The average nematic order  $\langle S \rangle$  is given as a colored

frame around these snapshots. At constant  $\Phi$ , as  $Pe$  increases, the system shows a continuous transition from an isotropic disordered state to one of relatively high nematic order, driven first by the formation of bundles, and then by the emergent network-like topology (see Fig. 6). Upon increasing  $\Phi$ , the transition to a reticulate pattern occurs at lower values of  $Pe$ , on account of the higher probability of the filaments to interact. We have previously shown [70] that the typical length scale of the reticulate pattern is directly connected to the curvature fluctuations; in our rescaled units, this predicted typical length  $\ell_{\text{pred}} = (\delta\kappa)^{-1} \propto Pe$ . Thus, as  $Pe$  increases, the characteristic size of the reticulate features increases.

We also explore the influence of filament length  $L$  on the system behavior, see Fig. 7. Changing the filament length can affect the area coverage  $\Phi$ , which, as demonstrated in Fig. 5, influences pattern selection. In these simulations we therefore modulate the number density  $\rho$ , to keep a constant area coverage of  $\Phi = 1$ . Changing the filament length  $L$  in this manner has no noticeable effect on the length scale of the emergent features. However, the resulting pattern is visually different. The longer filaments retain correlations in the patterns over longer times (the time it takes them to traverse their own length), leading to more fibrous-looking bundles. Shorter filaments, in contrast, produce denser bundles that show a stronger contrast in local density, when compared to inter-bundle regions; this is quantified by the more structured pair correlation function, see below.

We can obtain more precise information about the effects of the filament length  $L$  in our model cyanobacteria system by considering the limiting behavior as  $L$  approaches zero. Figure 8 shows how the average nematic order parameter  $\langle S \rangle$  depends on the Péclet number for different  $L$ . Generally, upon increasing  $Pe$  the system transitions from an isotropic state, characterized by a vanishingly small value of  $\langle S \rangle$ , to a reticulate pattern, characterized by  $\langle S \rangle \simeq 0.7$ . The transition point can be identified with the inflection point of the curve at  $Pe = Pe_c \simeq 1.8$ , which does not significantly change with filament length  $L$ . The spatial extent of the filaments effectively introduces memory into the system. So, while the chance of interacting with another filament remains the same, for a constant  $\Phi$ , the result of an aligning interaction will be retained within the system for a time  $L/v_0$ . This fact enables longer filaments to retain some degree of local order, even if the system is isotropic at larger scales. The nature of the observed phase transition thus changes with increasing filament length. Short filaments experience a sharper transition from disordered to ordered states while longer filaments experience a much smoother transition around this point. In the limit  $L \rightarrow 0$ , the system for  $\Phi = 1$  appears to approach a second-order or continuous transition at an apparent critical point  $Pe_c \simeq 1.8$ . The characterization of the critical scaling in the proximity of  $Pe_c$  is deferred

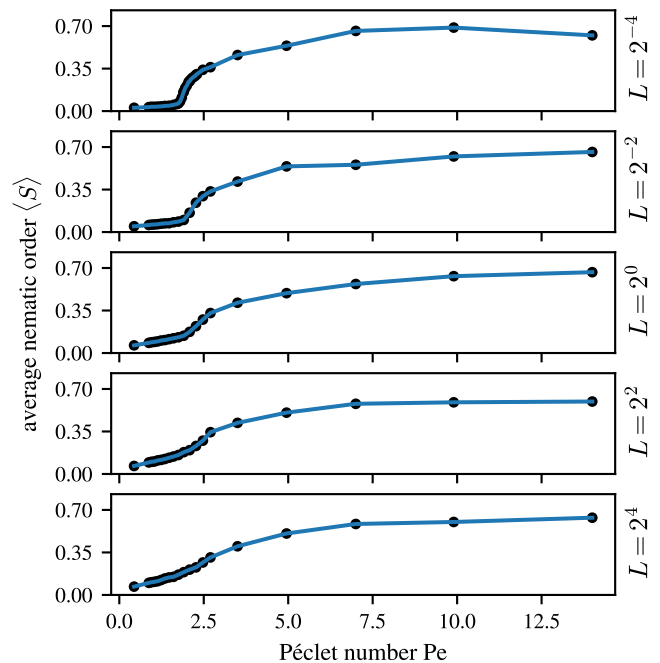


FIG. 8. Average nematic order parameter  $\langle S \rangle$  as a function of Péclet number, calculated as a block-average using  $1 \times 1$  sized blocks at different filament lengths  $L$ . The number of filaments is adjusted to ensure an equal area coverage of  $\Phi = 1$ , across all panels. With decreasing  $L$ , the transition from disorder to order takes on the appearance of a continuous transition.

to future work.

A powerful method to obtain structural information in soft-matter systems is the pair correlation function (PCF)  $g(r)$  [86]. This is defined as the probability of finding another particle within a volume  $dV$  at distance  $r$  from a reference particle. In polymer physics, it is possible to compute the PCF for any pair of monomers within the same chain or between different chains [87]. In our system, a simple choice is to consider the head-head PCF, where only the head bead of each filament is considered. Furthermore, given the long persistence length of the filament it is convenient to consider  $g(r)$  along the directions parallel and normal to the direction of motion of the filament's head. We thus define

$$g_{\parallel}(r) = \frac{1}{2\rho N_t w \Delta r} \left\langle \sum_{i,j} \delta(|(\mathbf{x}_i - \mathbf{x}_j) \cdot \mathbf{t}_i^0| - r) \right\rangle, \quad (9)$$

$$g_{\perp}(r) = \frac{1}{2\rho N_t w \Delta r} \left\langle \sum_{i,j} \delta(|(\mathbf{x}_i - \mathbf{x}_j) \times \mathbf{t}_i^0| - r) \right\rangle, \quad (10)$$

as the head-head parallel ( $\parallel$ ) and perpendicular ( $\perp$ ) PCF, respectively. In Eq. (9)-(10)  $\delta(r)$  is the Dirac delta distribution, the sums extend to all distinct pairs of filaments  $i$  and  $j$ , and  $\mathbf{t}_i^0$  is the tangent unit vector to the head



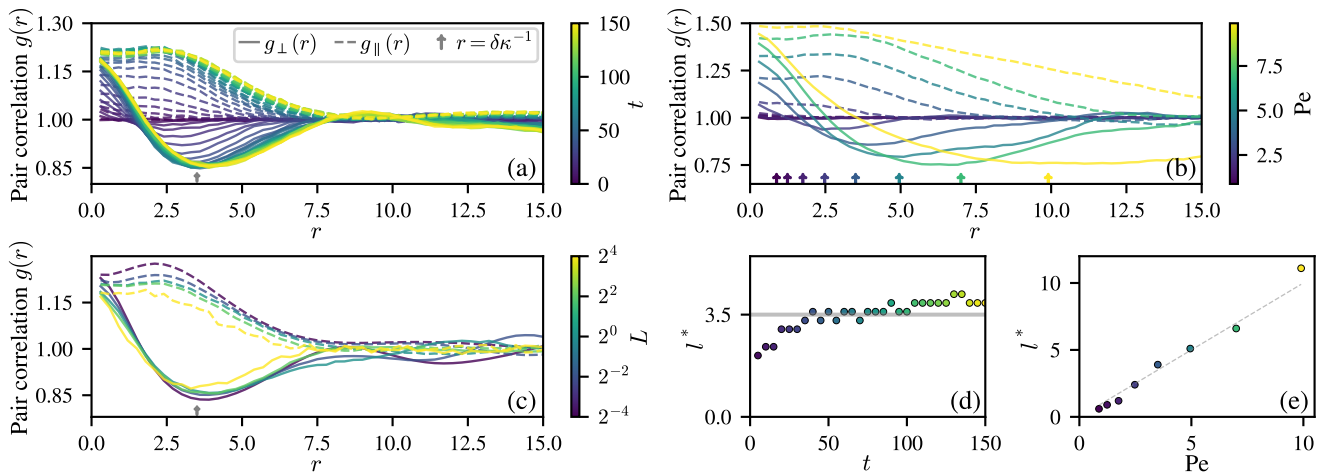


FIG. 9. Filament head-head pair correlation functions (PCFs) parallel to the direction of motion,  $g_{\parallel}(r)$  (dashed lines), and orthogonal to it,  $g_{\perp}(r)$  (solid lines), see Eqs. (9)-(10) quantify the structure of the reticulate pattern. (a) The time evolution (color axis) of these functions is shown for a system with area coverage  $\Phi = 1$ , filament length  $L = 1$  and Péclet number  $Pe = 3.5$ . As time advances and the reticulate pattern forms,  $g_{\parallel}(r)$  and  $g_{\perp}(r)$  converge to a steady state. For a system with a distribution of curvatures  $\delta\kappa$ , the minimum of  $g_{\perp}(r)$  coincides with  $Pe = (v_0\tau\delta\kappa)^{-1}$ , indicated by an arrow on the  $x$ -axis. (b) Steady-state PCFs are shown for different Péclet numbers  $Pe$ , keeping filament length  $L = 1$  and  $\Phi = 1$ . The minima in  $g_{\perp}(r)$  coincide with the length scales predicted from the distributions of curvatures, indicated by color-coded arrows. The shoulder in  $g_{\parallel}(r)$  moves to larger distances with increasing  $Pe$  (except for  $Pe = 9.9$ , where finite size effects are visible). (c) Effect of filament length  $L$  (color bar) on the PCFs at  $Pe = 3.5$ . The number density  $\rho$  is scaled here, to fix  $\Phi = 1$ . Independent of  $L$ , the minimum in  $g_{\perp}(r)$  coincides with the system's Péclet number, as denoted by an arrow. The magnitude of the extrema in  $g_{\parallel}$  and  $g_{\perp}$  decrease with increasing filament length, indicating less well-defined patterns. (d) Temporal evolution of the typical length scale  $\ell^*$  associated to the reticulate pattern, obtained from the minimum of  $g_{\perp}(r)$  in panel (a). At long times,  $\ell^* \rightarrow 3.5$ , which is the value of  $Pe$ . (e) Dependence of  $\ell^*$  on  $Pe$  showing that the minimum of  $g_{\perp}(r)$  matches the Péclet number and is a good measure of the reticulate's typical length scale; the dashed line corresponds to the identity.

bead; we sample filaments' heads within a narrow rectangle of width  $w = 10\sigma$  either parallel or perpendicular to the reference filament's head, and discretize the scalar distance  $r$  in bins of size  $\Delta r$ .

Figure 9(a) shows the emergence of the reticulate structure over time, as quantified by  $g_{\parallel}(r)$  and  $g_{\perp}(r)$ . As the system starts in an isotropic state (see Fig. 2), initially  $g_{\parallel}(r) = g_{\perp}(r) = 1$ . As the reticulate pattern forms,  $g_{\parallel}(r)$  develops a pronounced shoulder, and  $g_{\perp}(r)$  develops a distinct minimum. The significance of these features can be related to the reticulate geometry. For example, moving forward from any particular filament's head, along the direction of its tangent vector, one will be more likely to find other heads so long as they are within a bundle of filaments. Once the bundle bends away,  $g_{\parallel}(r)$  will decrease. This is reflected in a shoulder in  $g_{\parallel}(r)$ . Considering instead exploring in the direction normal to the path of a reference filament's head, one is also more likely to find other heads, but only so long as they are within the same bundle of filaments. As the bundles are relatively narrow, this probability decays quickly and drops below one in the regions between bundles, but then grows back when another bundle is encountered; this arrangement produces a minimum in  $g_{\perp}(r)$ . The position  $\ell^*$  of this minimum correlates with the pattern's

length scale; as the pattern coarsens, the depth of the minimum in  $g_{\perp}(r)$  and height of the shoulder in  $g_{\parallel}(r)$  increase, indicating the growth of the pattern length scale, as was observed in Fig. 2. The position of the minimum eventually settles on a value close to that of  $\ell_{\text{pred}} = Pe$ .

Upon increasing  $Pe$ , the position and magnitude of the shoulder in  $g_{\parallel}(r)$  and the minimum in  $g_{\perp}(r)$  grow, see Fig. 9(b). Simulations performed at the highest Péclet numbers show some finite size effects, as the scale of the pattern becomes comparable to the simulation domain. The prediction that the reticulate pattern's length scale is determined by the width of the curvature distribution  $\delta\kappa$  [70] holds throughout these simulations, as shown by the position of the shoulder of  $g_{\parallel}(r)$  and the minimum of  $g_{\perp}(r)$ . The filament length  $L$  has seemingly no influence on the typical scale of the emerging pattern. However, ordered and disordered regions are more clearly separated for shorter filaments (Fig. 9(c)), as evident in the more pronounced structure of both parallel and perpendicular PCFs.

Figure 9(d)-(e) show the dependence of  $\ell^*$  on time and Péclet number, respectively, as based on the results in Fig. 9(a)-(b). The position of the minimum of  $g_{\perp}(r)$  converges to the Péclet number of the simulation, which in our rescaled units, corresponds to the prediction for

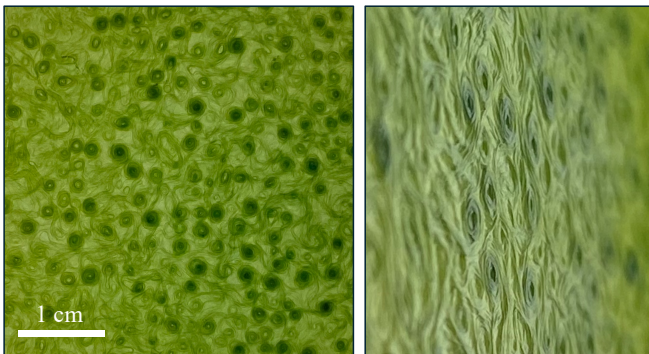


FIG. 10. *O. lutea* grown on agar for six months shows a more complex, three-dimensional structure. Photographs of the top surface of the biofilm (left panel: face-on view; right panel: tilted view) shows a complex topography of raised, filled circular features, which develop out of an earlier template of a more open, reticulate structure.

the length scale of the pattern  $\ell_{\text{pred}} = \text{Pe}$  [70].

## CONCLUSIONS AND OUTLOOK

We have studied the dynamics and structural properties of a colony of filamentous cyanobacteria as they undergo a topological transition to a reticulate pattern, a disordered network-like organization of filaments within bundles that link together. Filamentous cyanobacteria constitute a new class of active matter, which we have termed *active spaghetti* [70], due to the path-tracking nature of their gliding motility. We derived the nondimensional equations for a minimal model of their behavior that is firmly grounded in experimental evidence. The model captures the transient dynamics leading to the formation of the reticulate pattern. It also predicts a crossover in the mean-square displacement of filaments between ballistic and diffusive regimes, which can be rationalized in terms of an effective diffusivity. We explored the dynamics for different filament lengths, and found that the order parameter appears to approach a second order or continuous phase transition in the limit of very short filaments. The Péclet number dictates the typical length scale of the patterns, and together with the area coverage  $\Phi$  describes the relevant fields of the nonequilibrium phase diagram for our system. Inspired by polymer physics, we introduced parallel and perpendicular pair correlation functions, which capture the fundamental structural properties of the reticulate bundles. In particular, the minimum of  $g_{\perp}(r)$  faithfully predicts the typical length scale of the pattern,  $\ell^*$ . These observations can help further understand the formation and properties of cyanobacterial biomats.

Biofilms and biomats are self-organized microbial communities that differentiate and develop phenotypic adaptation both in space and time [8]. It stands to reason

that the form of the reticulate patterns studied here has a biological function sculpted by survival needs. The reticulate network then serves as a foundation for mature biofilms that adapt to the features of the surrounding environment. Because gliding cyanobacteria are surface associated, a natural question is to inquire how the surface properties influence the growth and maturation of the biofilm [88, 89]. As an initial exploration of the effects of substrate stiffness on colony formation, we also cultivated *O. lutea* on agar plates, see Fig. 10. These were prepared by mixing 1.5% agar, by weight, with a 1:50 dilution of BG11 broth in deionized water, following the protocols of Ref. [90]. Every eight weeks, 2 ml of 1:100 BG11 broth were added to the plates. Samples were otherwise left undisturbed, growing under identical conditions to those described for the transient experiment (Fig. 2), and following Ref. [70]. Over time, the initially reticulate pattern developed into a three-dimensional structure, with the open areas of the network filling in and growing upward that was templated on the original network boundaries. These observations point at the physical richness of this biological system and invite future exploration.

## ACKNOWLEDGMENTS

We thank Maike Lorenz (SAG Göttingen) for support with cyanobacteria cultures, Stefan Karpitschka from Max Planck Institute for Dynamics and Self-organisation (MPIDS) and Jack Paget (Loughborough) for discussions, and Graham Hickman (NTU) for microscopy support. We gratefully acknowledge Ellen Nisbet (University of Nottingham) for helpful discussions. Microscopy facilities were provided by the Imaging Suite at the School of Science and Technology at Nottingham Trent University. Numerical calculations were performed using the Sulis Tier 2 HPC Platform funded by EPSRC Grant EP/T022108/1 and the HPC Midlands+ consortium. We gratefully acknowledge use of the Lovelace HPC service at Loughborough University. M.K.F. was partly sponsored by the Malawi University of Science and Technology. This work was supported by the MPIDS. J.C. was supported by EPSRC grant EP/W522569/1 and UKRI/Wellcome grant no EP/T022000/1–PoLNET3. N.D. was supported by a BBSRC doctoral training programme (BB/T0083690/1).

## AUTHOR CONTRIBUTIONS

J.C. developed the simulation model and performed the simulations. M.K.F. and N.D. performed experiments. L.G. designed experiments. J.C., L.G., and M.G.M. designed the research. J.C., L.G., and M.G.M. wrote the manuscript with inputs from all authors.

## COMPETING INTERESTS

The authors declare no competing interests.

## CODE AVAILABILITY

The simulation code is available upon reasonable request.

---

\* E-mail: lucas.goehring@ntu.ac.uk

† E-mail: m.g.mazza@lboro.ac.uk

- [1] H. R. Maturana, The organization of the living: A theory of the living organization, *Int. J. Man-Machine Studies* **7**, 313 (1975).
- [2] S. A. Kauffman, Antichaos and adaptation, *Scientific American* **265**, 78 (1991).
- [3] S. A. Kauffman, *The origins of order: Self-organization and selection in evolution* (Oxford University Press, USA, 1993).
- [4] E. Karsenti, Self-organization in cell biology: a brief history, *Nat. Rev. Mol. Cell Biol.* **9**, 255 (2008).
- [5] J. R. Yates III, A. Gilchrist, K. E. Howell, and J. J. M. Bergeron, Proteomics of organelles and large cellular structures, *Nat. Rev. Mol. Cell Biol.* **6**, 702 (2005).
- [6] Y. Shibata, J. Hu, M. M. Kozlov, and T. A. Rapoport, Mechanisms shaping the membranes of cellular organelles, *Annu. Rev. Cell Dev. Biol.* **25**, 329 (2009).
- [7] M. J. Shelley, The dynamics of microtubule/motor-protein assemblies in biology and physics, *Annu. Rev. Fluid Mech.* **48**, 487 (2016).
- [8] P. Stoodley, K. Sauer, D. G. Davies, and J. W. Costerton, Biofilms as complex differentiated communities, *Annu. Rev. Microbiol.* **56**, 187 (2002).
- [9] M. G. Mazza, The physics of biofilms—an introduction, *J. Phys. D: Appl. Phys.* **49**, 203001 (2016).
- [10] K. Sauer, P. Stoodley, D. M. Goeres, L. Hall-Stoodley, M. Burmølle, P. S. Stewart, and T. Bjarnsholt, The biofilm life cycle: expanding the conceptual model of biofilm formation, *Nat. Rev. Microbiol.* **20**, 608 (2022).
- [11] W. Bialek, A. Cavagna, I. Giardina, T. Mora, E. Silvestri, M. Viale, and A. M. Walczak, Statistical mechanics for natural flocks of birds, *Proc. Natl. Acad. Sci. USA* **109**, 4786 (2012).
- [12] A. Cavagna and I. Giardina, Bird flocks as condensed matter, *Annu. Rev. Condens. Matter Phys.* **5**, 183 (2014).
- [13] Y. Katz, K. Tunstrøm, C. C. Ioannou, C. Huepe, and I. D. Couzin, Inferring the structure and dynamics of interactions in schooling fish, *Proc. Natl. Acad. Sci. USA* **108**, 18720 (2011).
- [14] S. Gueron and S. A. Levin, Self-organization of front patterns in large wildebeest herds, *J. Theor. Biol.* **165**, 541 (1993).
- [15] I. D. Couzin and J. Krause, Self-organization and collective behavior in vertebrates, *Advances in the Study of Behavior* **32**, 1 (2003).
- [16] T. Vicsek, A. Czirók, E. Ben-Jacob, I. Cohen, and O. Shochet, Novel type of phase transition in a system of self-driven particles, *Phys. Rev. Lett.* **75**, 1226 (1995).
- [17] J. Toner and Y. Tu, Long-range order in a two-dimensional dynamical XY model: how birds fly together, *Phys. Rev. Lett.* **75**, 4326 (1995).
- [18] R. A. Simha and S. Ramaswamy, Hydrodynamic fluctuations and instabilities in ordered suspensions of self-propelled particles, *Phys. Rev. Lett.* **89**, 058101 (2002).
- [19] S. Ramaswamy, The mechanics and statistics of active matter, *Annu. Rev. Condens. Matter Phys.* **1**, 323 (2010).
- [20] M. C. Marchetti, J.-F. Joanny, S. Ramaswamy, T. B. Liverpool, J. Prost, M. Rao, and R. A. Simha, Hydrodynamics of soft active matter, *Rev. Mod. Phys.* **85**, 1143 (2013).
- [21] J. Elgeti, R. G. Winkler, and G. Gompper, Physics of microswimmers—single particle motion and collective behavior: a review, *Rep. Prog. Phys.* **78**, 056601 (2015).
- [22] M. Fruchart, R. Hanai, P. B. Littlewood, and V. Vitelli, Non-reciprocal phase transitions, *Nature* **592**, 363 (2021).
- [23] X.-Q. Shi and H. Chaté, Self-propelled rods: linking alignment-dominated and repulsion-dominated active matter, arXiv:1807.00294v2 (2018).
- [24] D. Needleman and Z. Dogic, Active matter at the interface between materials science and cell biology, *Nat. Rev. Mater.* **2**, 1 (2017).
- [25] A. Doostmohammadi, J. Ignés-Mullol, J. M. Yeomans, and F. Sagués, Active nematics, *Nat. Commun.* **9**, 3246 (2018).
- [26] C. Bechinger, R. Di Leonardo, H. Löwen, C. Reichhardt, G. Volpe, and G. Volpe, Active particles in complex and crowded environments, *Rev. Mod. Phys.* **88**, 045006 (2016).
- [27] M. J. Bowick, N. Fakhri, M. C. Marchetti, and S. Ramaswamy, Symmetry, thermodynamics, and topology in active matter, *Physical Review X* **12**, 010501 (2022).
- [28] M. Bär, R. Großmann, S. Heidenreich, and F. Peruani, Self-propelled rods: Insights and perspectives for active matter, *Ann. Rev. Cond. Matt. Phys.* **11**, 441 (2020).
- [29] F. Ginelli, F. Peruani, M. Bär, and H. Chaté, Large-scale collective properties of self-propelled rods, *Physical review letters* **104**, 184502 (2010).
- [30] A. Baskaran and M. C. Marchetti, Enhanced diffusion and ordering of self-propelled rods, *Phys. Rev. Lett.* **101**, 268101 (2008).
- [31] T. Vicsek and A. Zafeiris, Collective motion, *Phys. Rep.* **517**, 71 (2012).
- [32] D. Martin, G. Spera, H. Chaté, C. Duclut, C. Nardini, J. Tailleur, and F. van Wijland, Fluctuation-induced first order transition to collective motion, arXiv preprint arXiv:2402.05078 (2024).
- [33] P. Romanczuk, M. Bär, W. Ebeling, B. Lindner, and L. Schimansky-Geier, Active brownian particles: From individual to collective stochastic dynamics, *Eur. Phys. J. Special Topics* **202**, 1 (2012).
- [34] A. P. Solon, M. E. Cates, and J. Tailleur, Active brownian particles and run-and-tumble particles: A comparative study, *Eur. Phys. J. Special Topics* **224**, 1231 (2015).
- [35] C. G. Wagner, M. F. Hagan, and A. Baskaran, Steady-state distributions of ideal active brownian particles under confinement and forcing, *J. Stat. Mech.: Theory Exp.* **2017** (4), 043203.
- [36] T. Sanchez, D. T. N. Chen, S. J. DeCamp, M. Heymann, and Z. Dogic, Spontaneous motion in hierarchically assembled active matter, *Nature* **491**, 431 (2012).

- [37] L. Giomi, Geometry and topology of turbulence in active nematics, *Phys. Rev. X* **5**, 031003 (2015).
- [38] T. B. Liverpool, A. C. Maggs, and A. Ajdari, Viscoelasticity of solutions of motile polymers, *Phys. Rev. Lett.* **86**, 4171 (2001).
- [39] R. E. Isele-Holder, J. Elgeti, and G. Gompper, Self-propelled worm-like filaments: spontaneous spiral formation, structure, and dynamics, *Soft Matter* **11**, 7181 (2015).
- [40] H. Jiang and Z. Hou, Motion transition of active filaments: rotation without hydrodynamic interactions, *Soft Matter* **10**, 1012 (2014).
- [41] Ö. Duman, R. E. Isele-Holder, J. Elgeti, and G. Gompper, Collective dynamics of self-propelled semiflexible filaments, *Soft Matter* **14**, 4483 (2018).
- [42] V. Bianco, E. Locatelli, and P. Malgaretti, Globulelike conformation and enhanced diffusion of active polymers, *Phys. Rev. Lett.* **121**, 217802 (2018).
- [43] S. K. Anand and S. P. Singh, Structure and dynamics of a self-propelled semiflexible filament, *Phys. Rev. E* **98**, 042501 (2018).
- [44] D. Saintillan, M. J. Shelley, and A. Zidovska, Extensile motor activity drives coherent motions in a model of interphase chromatin, *Proc. Natl. Acad. Sci. USA* **115**, 11442 (2018).
- [45] A. Joshi, E. Putzig, A. Baskaran, and M. F. Hagan, The interplay between activity and filament flexibility determines the emergent properties of active nematics, *Soft Matter* **15**, 94 (2019).
- [46] A. Martín-Gómez, T. Eisenstecken, G. Gompper, and R. G. Winkler, Active brownian filaments with hydrodynamic interactions: Conformations and dynamics, *Soft matter* **15**, 3957 (2019).
- [47] Y. Fily, P. Subramanian, T. M. Schneider, R. Chelakkot, and A. Gopinath, Buckling instabilities and spatio-temporal dynamics of active elastic filaments, *J. R. Soc. Interface* **17**, 20190794 (2020).
- [48] G. A. Vliegenthart, A. Ravichandran, M. Ripoll, T. Auth, and G. Gompper, Filamentous active matter: Band formation, bending, buckling, and defects, *Science advances* **6**, eaaw9975 (2020).
- [49] R. G. Winkler and G. Gompper, The physics of active polymers and filaments, *J. Chem. Phys.* **153**, 040901 (2020).
- [50] M. S. E. Peterson, M. F. Hagan, and A. Baskaran, Statistical properties of a tangentially driven active filament, *J. Stat. Mech.: Theory Exp.* **2020** (1), 013216.
- [51] A. Deblais, A. C. Maggs, D. Bonn, and S. Woutersen, Phase separation by entanglement of active polymerlike worms, *Phys. Rev. Lett.* **124**, 208006 (2020).
- [52] G. Du, S. Kumari, F. Ye, and R. Podgornik, Model of metameric locomotion in smooth active directional filaments with curvature fluctuations, *EPL* **136**, 58003 (2022).
- [53] L. Abbaspour, A. Malek, S. Karpitschka, and S. Klumpp, Effects of direction reversals on patterns of active filaments, *Phys. Rev. Res.* **5**, 013171 (2023).
- [54] T. Strübing, A. Khosravanizadeh, A. Vilfan, E. Bodenschatz, R. Golestanian, and I. Guido, Wrinkling instability in 3D active nematics, *Nano Lett.* **20**, 6281 (2020).
- [55] R. E. Blankenship, Early evolution of photosynthesis, *Plant Physiol.* **154**, 434 (2010).
- [56] T. Cardona, P. Sánchez-Baracaldo, A. W. Rutherford, and A. W. Larkum, Early archean origin of photosystem II, *Geobiol.* **17**, 127 (2019).
- [57] P. Sánchez-Baracaldo, G. Bianchini, J. D. Wilson, and A. H. Knoll, Cyanobacteria and biogeochemical cycles through Earth history, *Trends Microbiol.* **30**, 143 (2022).
- [58] M. Bižić, T. Klintzsch, D. Ionescu, M. Y. Hindiye, M. Günthel, A. M. Muro-Pastor, W. Eckert, T. Ulrich, F. Keppler, and H.-P. Grossart, Aquatic and terrestrial cyanobacteria produce methane, *Sci. Adv.* **6**, eaax5343 (2020).
- [59] D. Y. Sumner, Late Archean calcite-microbe interactions: two morphologically distinct microbial communities that affected calcite nucleation differently, *Palaios* **12**, 302 (1997).
- [60] C. F. Demoulin, Y. J. Lara, L. Cornet, C. François, D. Baurain, A. Wilmotte, and E. J. Javaux, Cyanobacteria evolution: Insight from the fossil record, *Free Radic. Biol. Med.* **140**, 206 (2019).
- [61] B. E. Schirrmeister, J. M. de Vos, A. Antonelli, and H. C. Bagheri, Evolution of multicellularity coincided with increased diversification of cyanobacteria and the great oxidation event, *Proc. Natl. Acad. Sci. USA* **110**, 1791 (2013).
- [62] J. M. Archibald, Endosymbiosis and eukaryotic cell evolution, *Current Biol.* **25**, R911 (2015).
- [63] P. W. Crockford, Y. M. B. On, L. M. Ward, R. Milo, and I. Halevy, The geologic history of primary productivity, *Curr. Biol.* **33**, 4741 (2023).
- [64] B. A. Whitton and M. Potts, Introduction to the cyanobacteria, in *Ecology of cyanobacteria II: their diversity in space and time* (Springer, 2012) pp. 1–13.
- [65] B. E. Schirrmeister, A. Antonelli, and H. C. Bagheri, The origin of multicellularity in cyanobacteria, *BMC Evol. Biol.* **11**, 45 (2011).
- [66] M. Scheffer, S. Rinaldi, A. Gragnani, L. R. Mur, and E. H. van Nes, On the dominance of filamentous cyanobacteria in shallow, turbid lakes, *Ecology* **78**, 272 (1997).
- [67] G. Markou and D. Georgakakis, Cultivation of filamentous cyanobacteria (blue-green algae) in agro-industrial wastes and wastewaters: a review, *Appl. Energy* **88**, 3389 (2011).
- [68] E. Hoiczky, Gliding motility in cyanobacteria: Observations and possible explanations, *Arch. Microbiol.* **174**, 11 (2000).
- [69] R. N. Shepard and D. Y. Sumner, Undirected motility of filamentous cyanobacteria produces reticulate mats, *Geobiology* **8**, 179 (2010).
- [70] M. K. Faluweki, J. Cammann, M. G. Mazza, and L. Goehring, Active spaghetti: collective organization in cyanobacteria, *Physical Review Letters* **131**, 158303 (2023).
- [71] M. Kurjahn, L. Abbaspour, F. Papenfuß, P. Bittihn, R. Golestanian, B. Mahault, and S. Karpitschka, Collective self-caging of active filaments in virtual confinement, *arXiv:2403.03093* (2024).
- [72] M. Kurjahn, A. Deka, A. Girot, L. Abbaspour, S. Klumpp, M. Lorenz, O. Bäumchen, and S. Karpitschka, Self-buckling of filamentous cyanobacteria reveals gliding forces, *arXiv:2202.13658* <https://doi.org/10.48550/arXiv.2202.13658> (2022).
- [73] A. Repula, C. Gates, J. C. Cameron, and I. I. Smalyukh, Photosynthetically-powered phototactic active nematic liquid crystal fluids and gels, *Commun. Mater.* **5**, 37 (2024).

- [74] X. Gong and M. Prakash, Active dislocations and topological traps govern dynamics of spiraling filamentous cyanobacteria, arXiv:2305.12572 (2023).
- [75] N. R. Franks, A. Worley, K. A. Grant, A. R. Gorman, V. Vizard, H. Plackett, C. Doran, M. L. Gamble, M. C. Stumpe, and A. B. Sendova-Franks, Social behaviour and collective motion in plant-animal worms, *Proceedings of the Royal Society B: Biological Sciences* **283**, 20152946 (2016).
- [76] V. Schaller, C. Weber, C. Semmrich, E. Frey, and A. R. Bausch, Polar patterns of driven filaments, *Nature* **467**, 73 (2010).
- [77] A. Del Mondo, G. Pinto, D. A. Carbone, A. Pollio, and A. De Natale, Biofilm architecture on different substrates of an oculatella subterranea (cyanobacteria) strain isolated from pompeii archaeological site (italy), *Environ. Sci. Pollut. Res.* **25**, 26079 (2018).
- [78] D. G. Cuadrado and J. Pan, Field observations on the evolution of reticulate patterns in microbial mats in a modern siliciclastic coastal environment, *J. Sediment. Res.* **88**, 24 (2018).
- [79] R. W. Castenholz, The behaviour of *Oscillatoria Terebriformis* in hot springs, *J. Phycol.* **4**, 132 (1968).
- [80] U. Pfreundt, J. Slomka, G. Schneider, A. Sen Gupta, F. Carrara, V. Fernandez, M. Ackermann, and R. Stocker, Controlled motility in the cyanobacterium trichodesmium regulates aggregate architecture, *Science* **380**, 830 (2023).
- [81] T. J. Mackey, D. Y. Sumner, I. Hawes, and A. D. Jungblut, Morphological signatures of microbial activity across sediment and light microenvironments of Lake Vanda, Antarctica, *Sediment. Geol.* **361**, 82 (2017).
- [82] S. A. M. Loos and S. H. L. Klapp, Irreversibility, heat and information flows induced by non-reciprocal interactions, *New J. Phys.* **22**, 123051 (2020).
- [83] M. Knežević, T. Welker, and H. Stark, Collective motion of active particles exhibiting non-reciprocal orientational interactions, *Sci. Rep.* **12**, 19437 (2022).
- [84] M. Nagy, Z. Ákos, D. Biro, and T. Vicsek, Hierarchical group dynamics in pigeon flocks, *Nature* **464**, 890 (2010).
- [85] A. Zöttl and H. Stark, Emergent behavior in active colloids, *J. Phys.: Condens. Matter* **28**, 253001 (2016).
- [86] J. G. Kirkwood and E. M. Boggs, The radial distribution function in liquids, *J. Chem. Phys.* **10**, 394 (1942).
- [87] B. H. Zimm, The scattering of light and the radial distribution function of high polymer solutions, *J. Chem. Phys.* **16**, 1093 (1948).
- [88] M. Krsmanovic, D. Biswas, H. Ali, A. Kumar, R. Ghosh, and A. K. Dickerson, Hydrodynamics and surface properties influence biofilm proliferation, *Adv. Colloid Interface Sci.* **288**, 102336 (2021).
- [89] A. A. Snowdon, S. P. Dennington, J. E. Longyear, J. A. Wharton, and P. Stoodley, Surface properties influence marine biofilm rheology, with implications for ship drag, *Soft Matter* **19**, 3675 (2023).
- [90] Culture Collection of Algae, SAG, Medium recipe vers. 10.2008, [http://sagdb.uni-goettingen.de/culture\\_media/01%20Basal%20Medium.pdf](http://sagdb.uni-goettingen.de/culture_media/01%20Basal%20Medium.pdf).